Correspondence

Power Prediction of PV Modules Contaminated by Bird Droppings via an Image Thresholding Process

Seong-Hyeon Ahn, *Fellow, IEEE*, Gyu Gwang Kim, Jin Ho Choi, Yeong-Beom Kang, Jin Hee Hyun, and Hyung-Keun Ahn, *Member, IEEE*

***Abstract*—Environmental factors that influence marine photovoltaic (PV) systems differ considerably from those affecting overland PV systems. The bird dropping, which is one of them, is a main cause of marine PV power reduction. The power prediction of a PV module contaminated by bird droppings is hard because light could pass through the bird dropping depending on the thickness of it unlike hard shading condition. This article shows differences between a bird-dropping shading and hard shading of the contaminated modules, and suggests a prediction model considering a transmittance of a bird dropping using image processing (IP). First, the shading rate (SR), which is the PV module surface ratio covered by bird droppings, is calculated using IP technologies. The accuracy of the SR is verified through an experiment creating artificial hard shading on the module using black masking tape. It has an error rate of 3% compared to our targeted benchmark SRs. Subsequently, an equivalent step methodology, which combines IV curves from individual cells to yield an IV curve for the entire PV module, was adopted to predict the power. The accuracy of this methodology is confirmed, and it showed a 5% error. However, in the case of real bird-dropping shades, discrepancies up to 15% are observed. In this article, the light penetration through bird droppings by a transmittance function was considered to predict the output of modules contaminated by the bird droppings. Errors fluctuate between 1%–20% based on the quantification of light interferences.**

***Index Terms*—Bird dropping, marine photovoltaics (PVs), operation and maintenance (O&M), transmittance.**

I. Introduction

With the expansion of photovoltaic (PV) installation, sites from land to floating and building integrated environments, specialized PV modules have been developed to fit their unique surroundings. Floating PV system offers numerous advantages, such as land use, limiting greenhouse effects, and providing cooling effects [1]. It is projected that by 2025, floating PVs will generate approximately 117 965 MWh of energy [1]. However, conventional PVs are limited in moist places owing to various factors. The moisture conditions accelerate the module degradation rates by transmitting vapor [2], [3], [4]. Water contamination occurs in FPV systems because of the leaching of Pb and other materials [5]. To address these challenges, advancements in PV modules have been made. For encapsulation, polyolefin elastomer can be used as an alternative to ethylene vinyl acetate owing to its reduced vapor transmission [3], [6]. Moreover, there are development in Pb-free PV options, such as lead-free perovskite PV and bus bars [7], [8].

Moreover, their applications can extend to marine environments, going beyond traditional settings with typical moisture levels found in dams, lakes, and reservoirs [1], [9]. Unlike freshwater environments, marine conditions pose their own challenges that must be solved [4], [9]. The challenges involve salty environments, wind and wave loads, and bird droppings. Salty environments are related to the long-term operation and maintenance (O&M) of marine PV, and the potentially induced degradation is accelerated by salty mist [10]. Salt crystals can be produced at the PV surface and decrease PV power and efficiency [11]. Wind and wave loads affect the mechanical systems of marine PV system. These loads can lead to microcracks and dealignments, and increase the costs of marine PV systems [4], [12], [13]. The shading effects of bird droppings are a major threat to marine PV operation. In some cases, seagulls and migratory birds use marine PV sites as their shelters. In terms of a PV maintenance, the impact of bird droppings immediately shows up as a reduction in power, whereas impacts of salty and mechanical loads take a relatively longer time to appear. Also, the bird dropping is mostly composed of a uric acid, which damages to a PV mechanical system [14].

Soiling loss is a main source of power loss due to shading. An experiment taken at Málaga University reported that maximum 15% and annually 6% of power reduction was measured owing to dirt soiling [15]. The transmittance of the soiling is an important parameter owing to the possibility of light penetration. Each soiling material has a different transmittance tendency. For instance, dry sand and glass result in an 11% degradation in transmittance, while dry bird droppings cause 54% degradation [16]. To model soiling as a form of soft shading, local dust properties and the relationship between transmittance and dust accumulation can simply be used [17]. Furthermore, the soiling loss has different tendencies depending on the region because salt particles can increase the cementation process [18]. Moisture can strengthen the adhesion of soiling particles, potentially leading to the formation of a strong crust [19]. The floating PV system is vulnerable to the crust because it is hard to be removed. The crust could also be formed by bird droppings resulting in additional power loss.

Bird droppings have a different transmittance and shading tendency compared to other types of depositions [16], [20]. For example, the degree of PV power loss varies depending on the tilt angle, as bird droppings may flow differently across the PV surface [20]. A power reduction could reach up to 23.8%, and the light transmittance of bird-dropping shades varies depending on the tilt angles [20]. A field test described that power reduction was correlated with the surface area of bird droppings [21]. Generalizing the power loss is challenging because the amount of deposition and its transmittance properties are hard to be quantified in experimental environments. This article aims to analyze and quantitatively assess the impact of severe bird droppings on power production in the context of O&M of a marine PV system.

Manuscript received 16 January 2024; accepted 2 February 2024. Date of publication 23 February 2024; date of current version 19 April 2024. This work was supported by the Human Resources Development Program of the Korea Institute of Energy Technology Evaluation and Planning grant funded by the Ministry of Trade, Industry and Energy, Republic of Korea under Grant RS-2023-00237035. *(Corresponding author: Hyung-Keun Ahn.)*

Seong-Hyeon Ahn, Yeong-Beom Kang, Jin Hee Hyun, and Hyung-Keun Ahn are with Next Generation Photovoltaic Module and Power System Research Center, Konkuk University, Seoul 05029, South Korea (e-mail: assadd99@konkuk.ac.kr; zee00966@naver.com; l6ky4122@konkuk.ac.kr; hkahn@konkuk.ac.kr).

Gyu Gwang Kim and Jin Ho Choi are with Chungbuk Technopark Next Generation Energy Center, Jincheon-gun 27872, South Korea (e-mail: rbrhkd00@cbtp.or.kr; jhchoi@cbtp.or.kr).

Color versions of one or more figures in this article are available at https://doi.org/10.1109/JPHOTOV.2024.3364811.

Digital Object Identifier 10.1109/JPHOTOV.2024.3364811

In this article, a method to generalize soiling loss due to bird droppings was proposed using image processing (IP) techniques. IP is widely used in the PV O&M field, particularly for PV fault detection, soiling analyses, and various PV applications. Mainly, image conversion to black-and-white, image thresholding, and color detection techniques are used. Additionally, thermal infrared images were also utilized by IP for PV fault detection because most faults influence the homogeneity of the temperature in PV. For example, hot spots in PV modules could be estimated by a thermal image thresholding [22]. An edge detection could be adapted to fault detection [23], [24]. Also, IP could be utilized for a maintenance of a PV system. For instance, IP can be effectively used to determine a reconfiguration of PV array by calculating a shading rate (SR) and increase the maximum power by 15% [25]. IP with a principle component analysis can be utilized to judge solar tracker faults [26].

IP techniques also facilitated an SR calculation of a soiling material. Image thresholding is universally used to calculate SR because it has a prominent calculation performance [27]. A PV clean cycle could be decided through a nonuniformity and estimation of dust concentration using IP [28]. Soiling concentration could be estimated by a neural network through a module image [29]. And the calculated soiling concentration is correlated with its transmittance [30]. In the field, it is totally impossible to get a soiling concentration value, so grayscale was used to solve the problem. Also, the SR or soiling level of dust could only be analyzed through IP. As floating and marine PVs are increasing worldwide, studies of the impact of bird droppings are needed. At present, there is a lack of sufficient studies that investigate both the transmittance of bird droppings and power prediction. This article describes those parts.

In this article, power predictions for PV module affected by bird droppings were conducted using the Bishop split (BS) model, which is a model that the illumination effects were applied to breakdown mechanisms [31]. The transmittance curve of bird droppings based on the grayscale was considered in this analysis. This article contributes to the following points.

1) A power comparison between the "hard shading" and bird-dropping shading is numerically described depending on SR.
2) Transmittances of bird-dropping samples are measured.
3) A function of transmittances and grayscales is proposed utilizing a black-and-white image.
4) Power prediction for modules covered by "soft shading" in aspect of optics is proposed.

The rest of this article is organized as follows. Section II introduces an IP method for the SR and its results. In Section III, the analyses of shaded PV outputs with calculated SR are presented. In Section IV, the transmittance of bird dropping shades are detected and a supplemental method for bird droppings is suggested. Finally, Section V concludes this article.

II. Shading Rate Calculated via Image Processing

This section describes the calculation process of SR using IP techniques, such as grayscale images and image thresholding. Although the images might contain noise factors, such as light reflection and resolution discrepancies, they were not considered severely in this article. IP was implanted by Python on Google CoLabs.

The test module and its equivalent circuit are illustrated in Fig. 1. The test module was custom-made for the marine environment by SHINSUNG E&G Co. The module shown in Fig. 1(a) is shingled, and its STC properties are listed in Table I, where *V*oc denotes the open-circuit voltage, *I*sc denotes the short-circuit current, *P*STC denotes the power at STC, and FF denotes the fill-factor. The test module has four bypass diodes, as shown in Fig. 1(b). Each bypass diode section contained 108 cutting cells, 6 parallel connections, and 18 series connections.

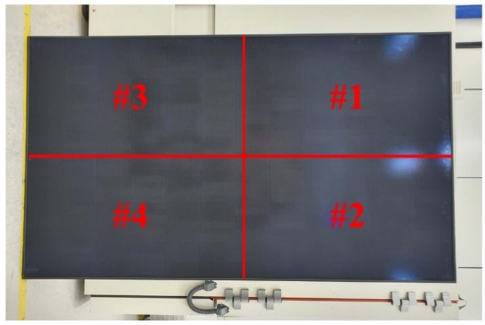

(a)

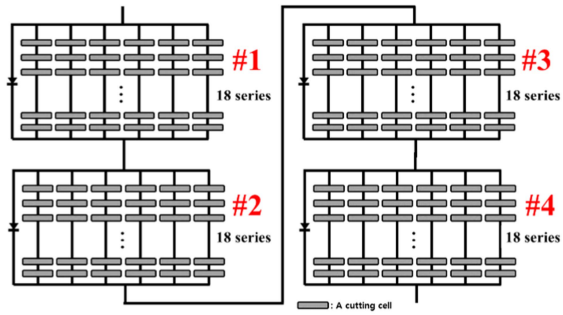

(b)

Fig. 1. Test module. (a) Entire module image. (b) Equivalent circuit.

TABLE I
STC Properties of a Test Module

Property	Value	Property	Value
V_{oc} $[V]$	48.14	I_{sc} $[A]$	11.08
P_{STC} $[W]$	419.67	FF [%]	78.69

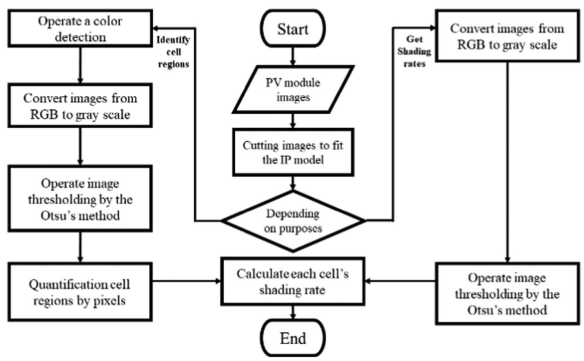

Fig. 2. Flow chart of the image processing for SR calculation.

A. Methodology

All module images used in this article were captured using the rear camera of the mobile phone, Galaxy Note 10 plus, which has a 12-mega pixel resolution. Then, they were edited to match their module size. The experiments were conducted at the laboratory located in the Chungbuk Technopark Next Generation Energy Center. Fig. 2 presents a flowchart of the IP used in this article. IP was performed in two categories:

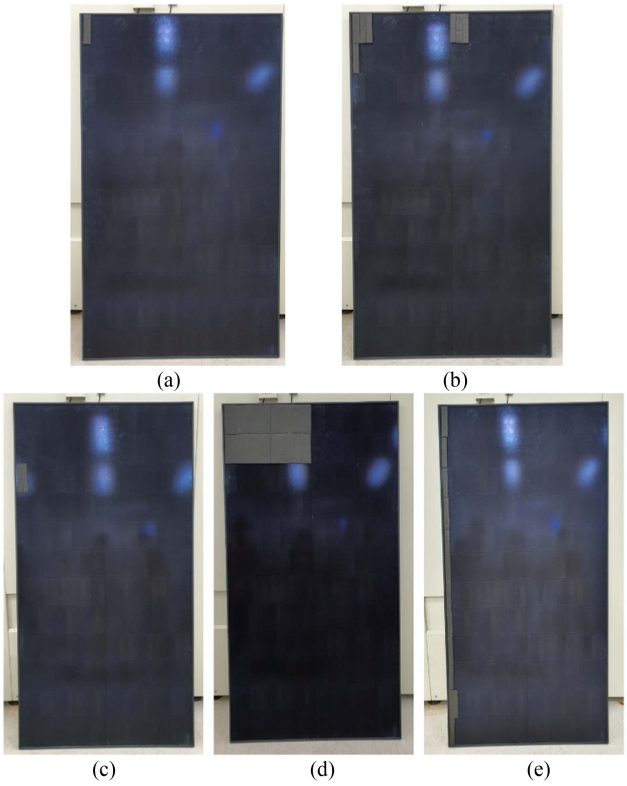

Fig. 3. Raw module images with artificial shades: (a) A1, (b) A2, (c) A3, (d) A4, and (e) A5.

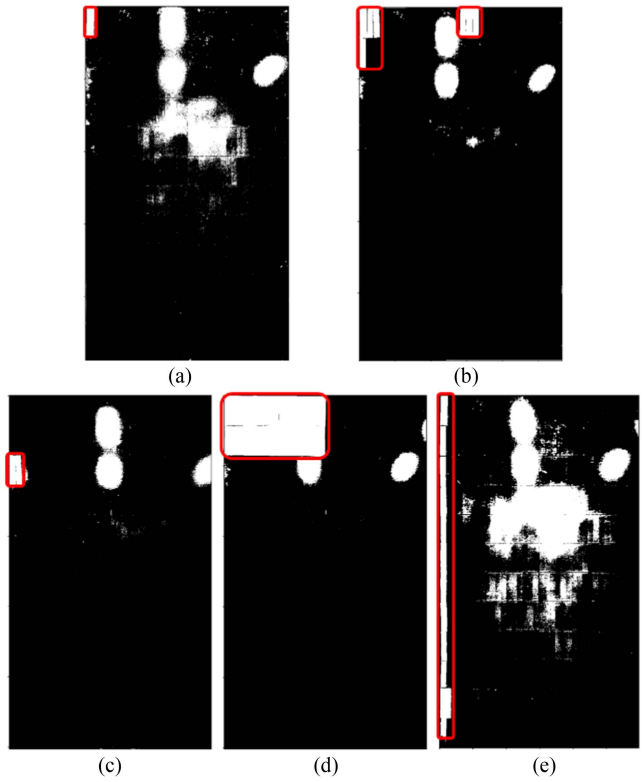

Fig. 4. Image thresholding results of artificial shades: (a) A1, (b) A2, (c) A3, (d) A4, and (e) A5.

distinguishing cell regions and SR computations. In this article, SR is defined as the ratio of the surface covered by bird droppings to the entire surface, as described in (1). A_{bd} denotes a surface covered by bird droppings and A_T denotes an entire surface. In both of categories, converting images to black-and-white and image thresholding were performed. Image thresholding is the process of separating grayscale based on a specific value and is conducted using the Otsu's method [32]

$$\mathrm{SR} = A_{\mathrm{bd}}/A_T. \tag{1}$$

B. Distinguishing Artificial Shades

Artificial shades were first used in the IP model. Artificial shades were made by a black masking tape in the test module and consisted of five cases, depicted in Fig. 3. The black tape was attached by checking a location and size of the cutting cell. Fig. 4 shows the results of the image thresholding of the artificial shades. The red boundaries in Fig. 4 depict the thresholding results for the artificial shades. Owing to external light sources, many noises, such as light reflections, appear, as shown in Fig. 4. This noise must be eliminated from the actual field.

Table II displays the outcomes of the SR analysis conducted both with and without noise. This analysis was conducted by translating the thresholding results into SR, on a cell-by-cell basis. The calculated SRs are derived from values within the red boundaries, excluding any noise. The derived SRs were then cross-validated by comparing them with targeted benchmarks. For instance, in comparing with Fig. 6(a), where only one cell was entirely shaded, the calculated SR is compared to the targeted SR matrix, [100,0,0,0, …,0]. As a result, the mean absolute percentage error corresponded to 0.05% and the root mean square error (RMSE) was 0.79%. Hence, the IP model can approximate the SR with an accuracy within 3% without light noise.

TABLE II
ANALYSIS OF ARTIFICIAL SHADING RATES

CASE	With noises		Without noises	
	MAPE (%)	RMSE (%)	MAPE (%)	RMSE (%)
A1	9.85	25.97	0.05	0.79
A2	3.57	14.95	0.32	2.63
A3	3.29	15.42	0.07	0.90
A4	1.98	11.14	0.16	0.87
A5	17.39	34.83	0.46	2.86

C. Distinguishing Bird Droppings

Given that the artificial shades were fabricated using black masking tapes, distinguishing them from the module surface became challenging, especially when compared with light reflections. Fig. 5 shows raw module images contaminated by bird droppings. Unlike the artificial shades, bird droppings are more discernible due to their brighter colors relative to the module surface. Fig. 6 illustrates the results of image thresholding for shades due to bird droppings. The modules depicted in Fig. 6 was positioned in a marine environment, in Saemangeum, South Korea (35.7°N 126.5°E). It is reported that 453 698 of birds inhabited in the installation site at 2009 [33]. Considering the orientation of these modules, traces of bird droppings were detected running from the top to the bottom.

Table III lists the calculated SR depending on the bypass diode sections (Fig. 1) and the total SR. The modules generally had a total SR between 24% and 33%, although their specific trial patterns were

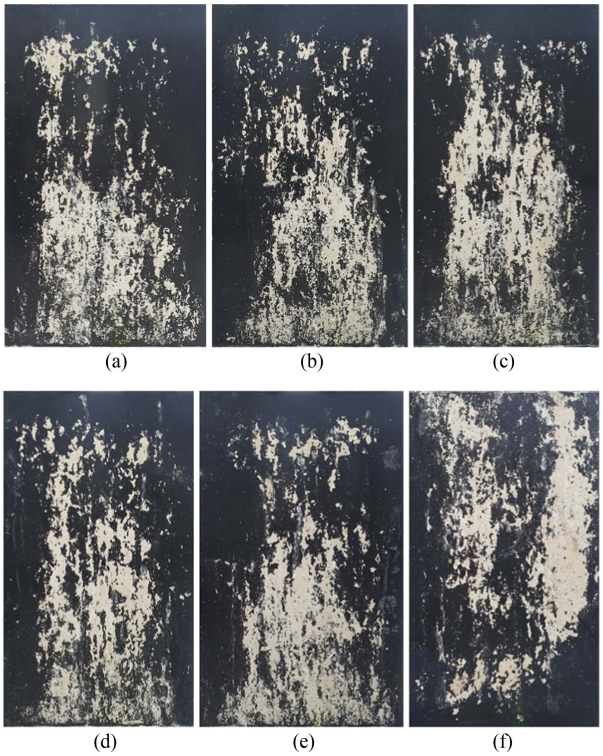

Fig. 5. Raw module images with bird-dropping shades: (a) M1, (b) M2, (c) M3, (d) M4, (e) M5, and (f) M6.

TABLE III
ANALYSIS OF BIRD-DROPPING SHADING RATES

CASE		SR (%)		Case		SR (%)	
M1	#1	16.61	24.60	M4	#1	21.11	26.30
	#2	5.68			#2	15.77	
	#3	40.02			#3	32.42	
	#4	36.09			#4	35.88	
M2	#1	15.52	24.66	M5	#1	11.75	27.18
	#2	13.90			#2	14.90	
	#3	25.59			#3	40.33	
	#4	43.65			#4	41.75	
M3	#1	25.95	30.73	M6	#1	36.60	32.86
	#2	17.34			#2	48.09	
	#3	37.82			#3	17.40	
	#4	41.84			#4	29.36	

different. M1 has bird-dropping shades of 16.61%, 5.68%, 40.02%, and 36.09%, depending on the bypass diode sections. M1–M5 exhibited similar bird-dropping trails; the bird droppings are concentrated in the lower part of the module (#3 and #4 bypass diode sections). In contrast, M6 had concentrated bird droppings in the upper part of the module(#1 and #2 bypass diode sections).

III. Power Prediction Model and Application

PV power prediction is performed using the SRs calculated in the previous section. Power prediction was performed by computing the maximum power in the IV curve. The power prediction was performed using MATLAB 2022b.

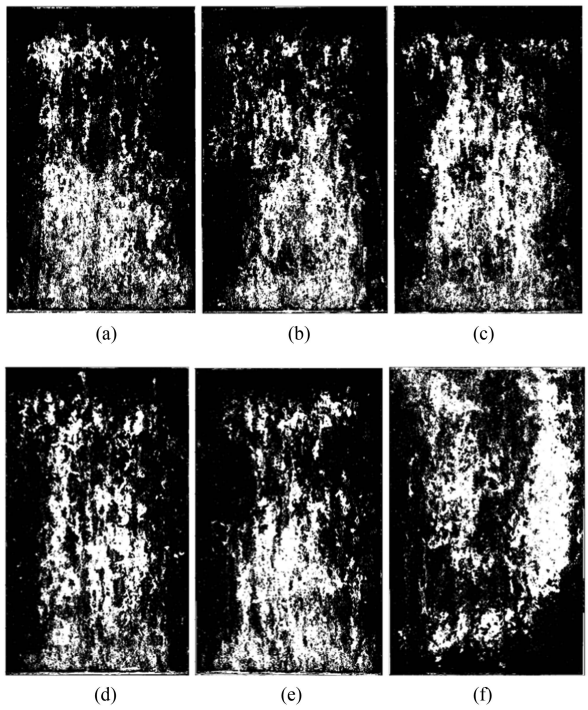

Fig. 6. Image thresholding results of bird-dropping shades: (a) M1, (b) M2, (c) M3, (d) M4, (e) M5, and (f) M6.

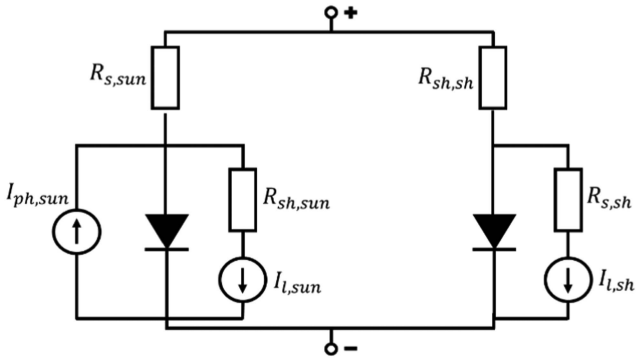

Fig. 7. Equivalent circuit of a Bishop split model.

A. Model Description

Power prediction of a shaded PV module must consider the operation of its bypass diodes for the power prediction accuracy. The bypass diodes triggered by the reverse bias voltages of shaded cells offer more power [34], [35], [36]. PV modules must include two or more bypass diodes to minimize power reduction due to shades. In this article, the operations of these bypass diodes were modeled by drawing IV curves from the cell units.

IV curves of shaded PV cells were drawn using the BS model. Specifically, BS is the Bishop model that applies illumination effects to breakdown mechanisms [31]. BS divides a PV cell into shaded and nonshaded region. Its equivalent circuit is shown in Fig. 7, and its associated equations range from (2) to (6). $I_{\rm sun}$, $I_{l,\rm sun}$, $R_{s,\rm sun}$, and $R_{\rm sh,sun}$ denote the operating current, leakage current, series resistance, and parallel resistance of the nonshaded region in BS, respectively. Similarly, $I_{\rm sh}$, $I_{l,\rm sh}$, $R_{s,\rm sh}$, and $R_{\rm sh,sh}$ denote the operating current, leakage current, series resistance, and parallel resistance, respectively, of the shaded region of BS. Specifically, $a_{\rm sun}$ and $a_{\rm sh}$ determine the rates

of ohmic current, and b_{sun} and b_{sh} are avalanche breakdown exponents. $I_{\text{ph,sun}}, I_o, V_T$, and n represent the photocurrent in the unshaded region, saturation current, thermal voltage, and ideality factor, respectively. I and V denote the total operating voltage and current of the BS

$$I_{\text{sun}} = I_{\text{ph,sun}} - I_o\left\{\exp\left(\frac{V + I_{\text{sun}}R_{s,\text{sun}}}{nV_T}\right) - 1\right\} - I_{l,\text{sun}} \tag{2}$$

$$I_{\text{sh}} = -I_o\left\{\exp\left(\frac{V + I_{\text{sh}}R_{s,\text{sh}}}{nV_T}\right) - 1\right\} - I_{l,\text{sh}} \tag{3}$$

$$I_{l,\text{sun}} = -\left(\frac{V + I_{\text{sun}}R_{s,\text{sun}}}{R_{\text{sh,sun}}}\right)\left\{1 + a_{\text{sun}}\left(1 - \frac{V + I_{\text{sun}}R_{s,\text{sun}}}{V_{\text{br,sun}}}\right)^{-b_{\text{sun}}}\right\} \tag{4}$$

$$I_{l,\text{sh}} = -\left(\frac{V + I_{\text{sh}}R_{s,\text{sh}}}{R_{\text{sh,sh}}}\right)\left\{1 + a_{\text{sh}}\left(1 - \frac{V + I_{\text{sun}}R_{s,\text{sh}}}{V_{\text{br,sh}}}\right)^{-b_{\text{sh}}}\right\} \tag{5}$$

$$I = I_{\text{sun}} + I_{\text{sh}}. \tag{6}$$

Series and parallel resistances were used separately according to the shaded region. Splitting each resistance from the STC is performed using (7)–(10) [31]. A_T denotes the cut cell size, A_{sun} denotes the nonshaded region in a cutting cell, and A_{sh} denotes the shaded region in a cutting cell. R_s and R_{sh} denote the series and parallel resistances under the STC. Given that R_s and R_{sh} were not measured (see Table I), the values of R_s and R_{sh} were fitted using the STC

$$R_{s,\text{sun}} = R_s \cdot \frac{A_T}{A_{\text{sun}}} \tag{7}$$

$$R_{\text{sh,sun}} = R_{\text{sh}} \cdot \frac{A_T}{A_{\text{sun}}} \tag{8}$$

$$R_{s,\text{sh}} = R_s \cdot \frac{A_T}{A_{\text{sh}}} \tag{9}$$

$$R_{\text{sh,sh}} = R_{\text{sh}} \cdot \frac{A_T}{A_{\text{sh}}}. \tag{10}$$

I_o is modeled by V_{oc} and I_{sc}, as shown in (11) [37]. $V_{\text{oc},o}$ and I_{ph} are the initial open-circuit voltage and photocurrent, respectively, when fully unshaded. In this article, it is assumed that I_{sc} is the same as I_{ph}, and the shading effects of V_{oc} and $I_{\text{ph,sun}}$ are considered as shown in as follows [38]:

$$I_o = \frac{I_{\text{sc}}}{\exp\left(V_{\text{oc}}/nV_T\right) - 1} \tag{11}$$

$$V_{\text{oc}} = V_{\text{oc},o} + nV_T \cdot \ln\left(1 - \text{SR}\right) \tag{12}$$

$$I_{\text{ph,sun}} = I_{\text{ph}} \cdot (1 - \text{SR}) \approx I_{\text{sc}} \cdot (1 - \text{SR}). \tag{13}$$

Table IV shows parameter values used in this article. A_T was calculated by dividing the number of cut cells by the entire module size. A breakdown voltage ($V_{\text{br,shade}}$) has generally between -20 and -30 V in a monocrystalline Si PV [39]. The values of $a_{\text{sun}}, a_{\text{sh}}, b_{\text{sun}}, b_{\text{sh}}$, and $V_{\text{br,sun}}$ were obtained from a previous article [31].

B. Power Prediction of Artificial and Bird-Dropping Shades

Fig. 8 shows a flowchart of the IV curve modeling. The SR and IV curves for each cell were calculated using the IP and BS model. Then, an IV curve of a PV module is calculated via "equivalence" steps. Equivalence operates differently depending on whether the circuit structure is in series or parallel. In the case of a series connection, the series cells are equalized to a single cell by combining the operating voltages of each cell at a certain current level. In parallel connections, parallel cells are equalized to a single cell by combining the operating current of each cell at a certain voltage level.

TABLE IV
VALUES OF MODEL PARAMETERS

Parameter	Value	Parameter	Value
$V_{\text{br, sun}}$ [V]	−70 598	$V_{\text{br, shade}}$ [V]	−29.74
a_{sun}	1	a_{sh}	0.01
b_{sun}	12 410	b_{sh}	2.06
R_s [Ω]	0.02	R_{sh} [Ω]	500
n	1	A_T [cm^2]	50.815

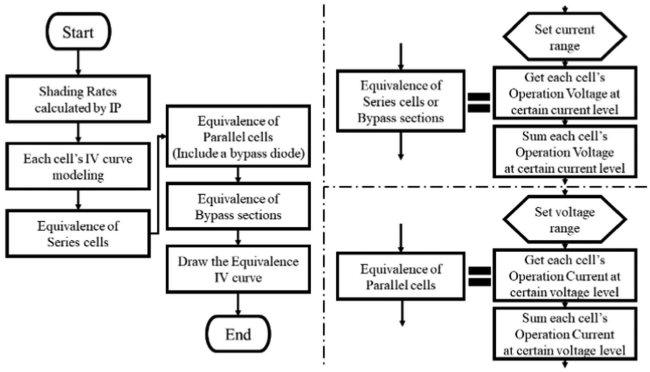

Fig. 8. Flow chart of the IV curve modeling.

TABLE V
ANALYSIS OF ARTIFICIAL SHADE POWER PREDICTION

Case	Predicted (W)	Measured (W)	Deviation (W)	APE (%)
No shade	423.26	419.67	3.59	0.86
A1	381.59	390.00	−8.41	2.16
A2	328.80	316.13	12.67	4.01
A3	377.15	380.75	−3.60	0.95
A4	310.80	312.41	−1.60	0.51
A5	189.08	196.36	−7.28	3.71

Fig. 9 shows IV curves of the artificial shades resulting from the prediction model. The simulated curves traced the measured curves well, however, a mismatch occurred when the current was low. This mismatch could be attributed to the weakness of one diode model; the recombination loss was not adequately considered [40].

Table V describes the numerical analysis (maximum power) of Fig. 9 depending on the case. The errors are greater than those of the IP model (see Table II), but within 5%.

Fig. 10 shows the IV curves of the bird-dropping shades. The simulated curves exhibit similar trends to the measured curves but relatively low values. Although the model works well in the artificial shade, a current of almost 1–2 A was underestimated in bird droppings.

Table VI presents the numerical analysis of Fig. 10 depending on the case. The maximum power of each case had a consistently lower value than the measured value, almost 10%–40% lower. Given that the power prediction model assumes a hard shading, it can predict the maximum power well in artificial shades. However, in the case of bird

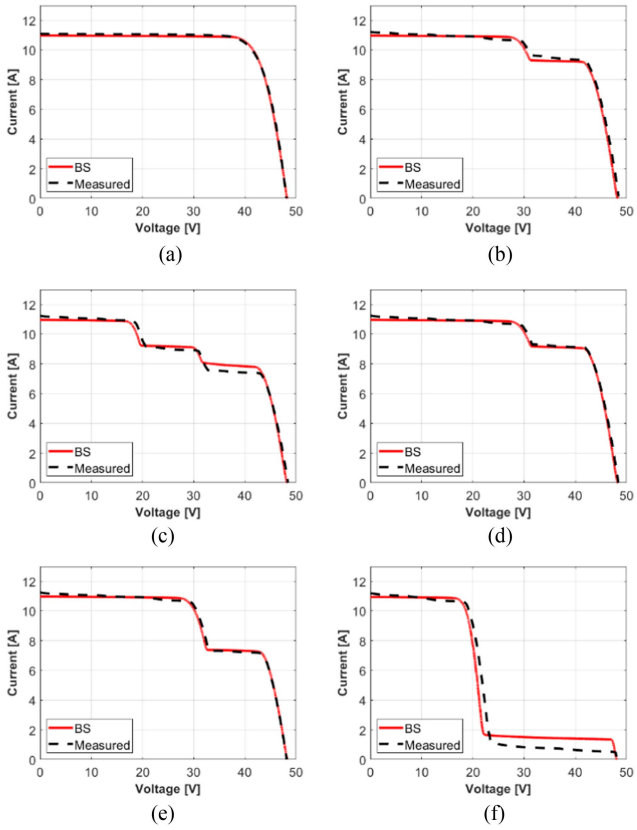

Fig. 9. IV curve results of artificial shades: (a) no shade, (b) A1, (c) A2, (d) A3, (e) A4, and (f) A5.

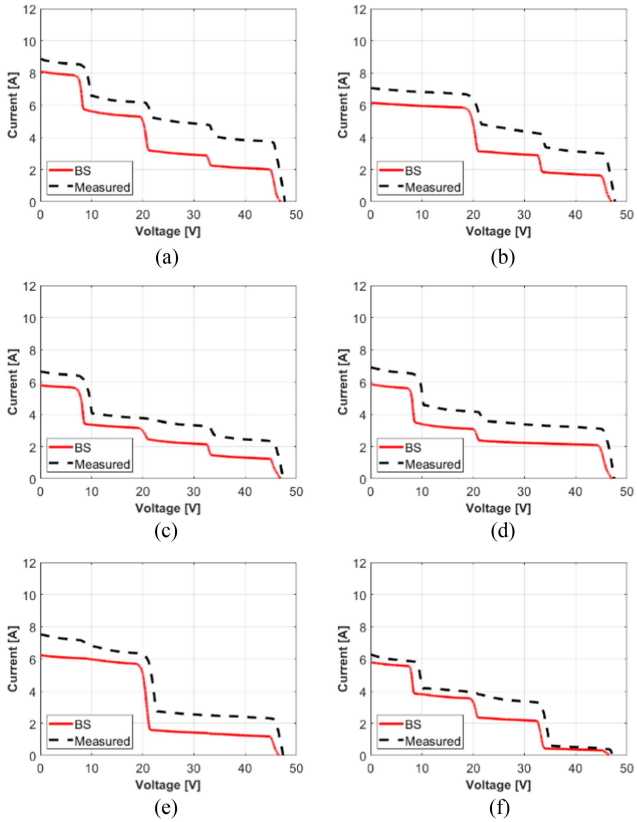

Fig. 10. IV curve results of bird-dropping shades: (a) M1, (b) M2, (c) M3, (d) M4, (e) M5, and (f) M6.

TABLE VI
ANALYSIS OF BIRD-DROPPING POWER PREDICTION

Case	Predicted [W]	Measured [W]	Deviation [W]	APE (%)
M1	103.54	167.01	−63.47	38.0
M2	108.25	135.82	−27.56	20.3
M3	69.46	103.08	−33.61	32.6
M4	92.16	138.71	−46.55	33.6
M5	107.63	127.02	−19.39	15.3
M6	69.59	107.50	−37.92	35.3

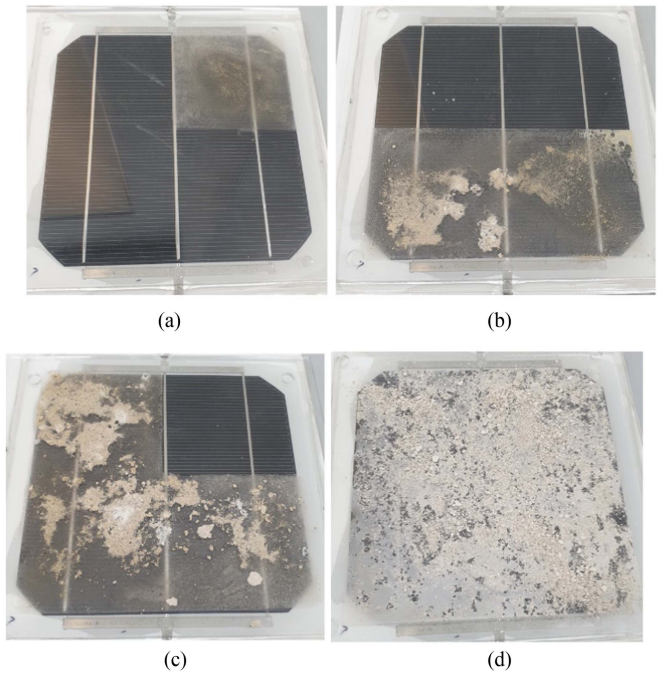

Fig. 11. Examples of one cell shaded by bird droppings: (a) 25% shaded, (b) 50% shaded, (c) 75% shaded, and (d) 100% shaded.

droppings, the results show that there is some photoelectric effect in the bird-dropping shade.

IV. Proposed Model for Bird Droppings

This section describes a supplementary process for understanding the properties of bird-dropping shades. First, analyses of bird-dropping shades, such as transmittance and power comparisons with hard shading, were conducted. This article proposes a method for predicting the maximum power of modules contaminated by bird droppings based on following analyses.

A. Transmittance Property of Bird-Dropping Shades

In the previous section, consistent errors were observed in the bird-dropping results, indicating the need to consider soft shading. To confirm that the bird-dropping shades are "soft-shading," we tested the variation in PV output between hard shading and bird droppings. Fig. 11 illustrates instances of a cell affected by bird-dropping shades. The shades mimicking bird droppings were created using a real bird-dropping solution. The solution is made by water (80 g) and solid bird droppings (40 g). Bird-dropping territories are divided by a double-sided tape, respectively, 25%, 50%, 75%, and 100% of a cell size.

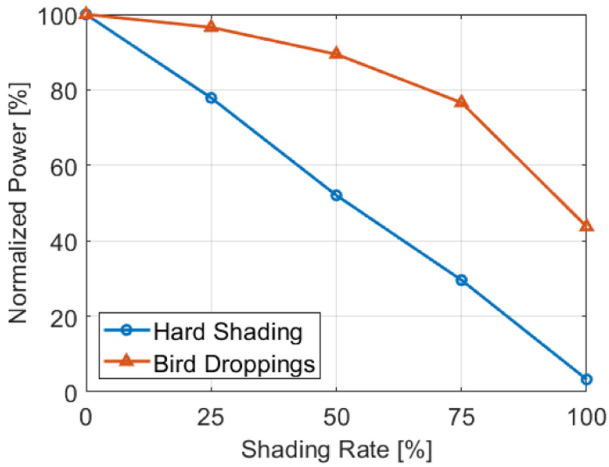

Fig. 12. Normalized power depending on the shading rate and type.

Because the bird dropping is composed of water-solubility materials and nonwater-solubility materials, a sediment must be existed in the solution. Although we stirred up the solution before pouring, the later-made bird-dropping patterns are largely influenced by the sediment. For comparison, hard-shading patterns, fabricated using black masking tape, were applied to identical areas where the simulated bird-dropping shades were present.

The power of the shaded cell for both bird droppings and hard shading was measured under the STC. Fig. 12 shows a comparison of the PV output depending on the SR and type. Based on the STC output of one cell, the normalized power of hard shading was proportional to the SRs of 77.87%, 52.05%, 29.59%, and 3.27%. Because light could pass through edges of the hard-shading pattens, higher power rates appear than SRs. However, in the case of bird droppings, larger outputs were measured at 96.56%, 89.44%, 76.61%, and 43.76%. Although a clear distinction between the dense bird-dropping regions and the shallow bird-dropping regions is observed in Fig. 11, a power deviation of approximately 40% is observed. In Fig. 11(d), the whole surface is covered by dense bird droppings, while the others have very shallow bird-dropping regions, and these regions could cause higher power generation due to light penetration. However, Fig. 11(d) has almost 40% of a STC power despite the overall dense bird droppings. These results indicate that light can pass through the shade created by bird droppings and generate more power.

The transmittance of various bird-dropping samples relative to the transmittance of a low-iron glass was tested to identify a correlation between the transmittance and thickness of bird droppings. Fig. 13(a) shows examples of low-iron glass covered with bird droppings, black tape, and without any covering. Owing to a black back sheet, a degree of thickness could be indirectly figured in case of the bird droppings. The left side of lower one seems to have the shallowest bird droppings. The left side of upper one seems to have the second shallowest and others are hard to judge. The dimensions of low-iron glass sheets were 50 mm × 50 mm × 3 mm. The red boundaries in Fig. 13(a) represent transmittance measurement areas using Solid Spec-3700i, SHIMADZU. Transmittances are measured from 280 to 1100 nm and are shown in Fig. 13(b), where the blue lines and red lines represent the left and right axes, respectively. Definitely, bird droppings have different transmittances depending on their thickness and distributional patterns.

The transmittance can be calculated using (14) based on the transmittance as a function of wavelength. T_W denotes the total transmittance of the sample, and t denotes the transmittance function as a function

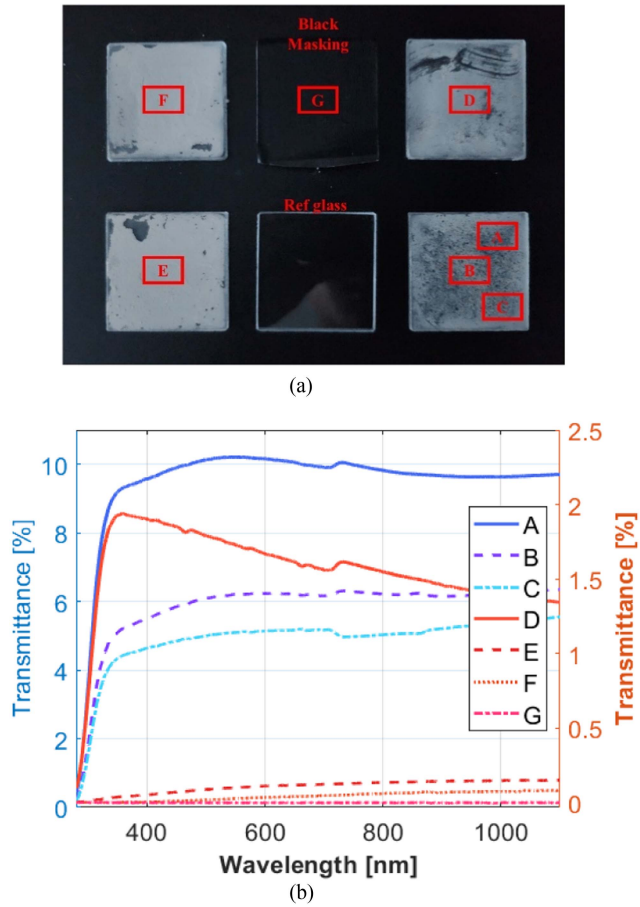

Fig. 13. Transmittance analyses by wavelengths: (a) measurement regions and (b) measured transmittances depending on the measurement regions.

of wavelength. Whole transmittances in Fig. 13(a) are 9.50%, 5.86%, 4.89%, 1.57%, 0.11%, 0.04%, and 0.00%. These transmittances are values considering both bird-droppings and low-iron glass. To solely account for bird droppings, the total transmittance is divided by the total transmittance of the low-iron glass, as shown in (15). T_R denotes a total transmittance unaffected by the low-iron glass and $T_{\text{low iron}}$ denotes the total transmittance of the low-iron glass. The transmittance of the low-iron glass is also measured by the same device. The unaffected transmittances in Fig. 13(a) are 10.98%, 6.77%, 5.65%, 1.81%, 0.13%, 0.05%, and 0.00%. Hence, there is a clear occurrence of light penetration, and the subsequent step involves modeling this phenomenon

$$T_W = \frac{1}{1100 - 280} \int_{280\text{ nm}}^{1100\text{ nm}} t\,(\lambda)\, d\lambda \tag{14}$$

$$T_R = T_W \,/\, \left(\frac{T_{\text{low iron}}}{100}\right). \tag{15}$$

B. Transmittance Depending on Grayscale

Transmittance is affected by various factors, such as the thickness and color of the material, and particle size. A supplementary analysis that considers all factors is difficult to model. Setting sensors to measure these factors creates an unnecessary budget for O&M. Also, a slight change of thickness could cause a large change of a transmittance. Therefore, we focused on the color of bird droppings, especially on gray scale, because the color of bird droppings is separated by the color

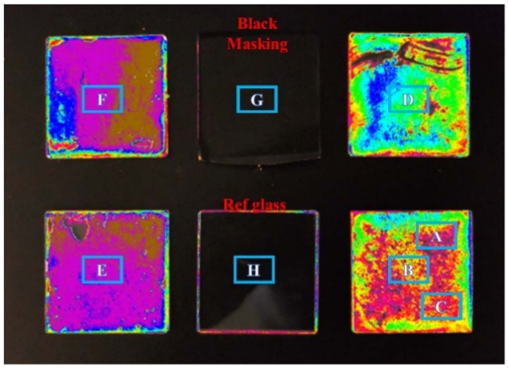

(a)

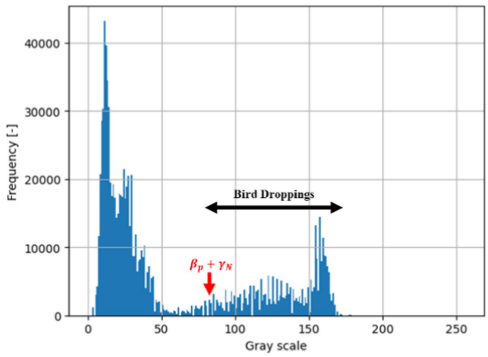

(b)

Fig. 14. Supplement analyses of a bird dropping image: (a) color conversion image from the gray image, and (b) image histogram of the gray image.

TABLE VII
COLOR CONVERSIONS BASED ON GRAYSCALE

Gray scale (-)	Conversion			
	Color	R	G	B
80–90		255	0	204
90–100		255	0	0
100–110		255	150	0
110–120		255	255	0
120–130		0	255	0
130–140		0	255	255
140–150		0	0	255
150–160		204	5	204
160–170		153	102	0
170~		255	255	255

of the module surface. If the bird drop is shallow, then the color of the module surface can pass through it. This implies that these regions exhibit relatively low grayscale in a black-and-white image. Conversely, if the bird-dropping thickness is large, the color of the module surface cannot pass through the bird droppings. This implies that these regions have a relatively large grayscale in the black-and-white images. Thus, we use the grayscale as a thickness of a bird dropping to utilize a relationship between a thickness and a transmittance.

Fig. 14(a) shows a color conversion image depending on the values of the grayscale used to identify the aforementioned statements. A rule of the color conversion is based on image histogram of the original image [Fig. 13(a)], when external light sources are minimized, and described in Table VII. Fig. 14(b) shows the image histogram. We determined that the grayscale region of the bird droppings is between 80 and 170,

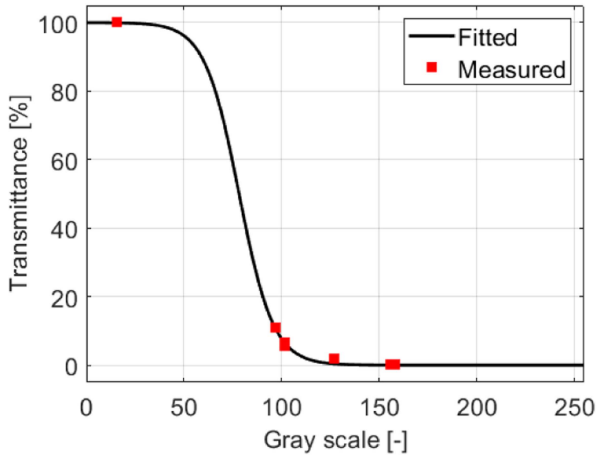

Fig. 15. Transmittance curve when light noise is minimized.

as shown in Fig. 14(b). The step size of the color conversion was set to 10. As a result, the high transmittance regions due to the shallow bird dropping have lower gray scale (darker) than the low transmittance regions.

The sky-blue boundary regions excluding "H" in Fig. 14(a) are same regions with the transmittance measurement regions, and the red boundary regions in Fig. 13(a). The "H" region is a transmittance measurement region of a low-iron glass. The averaged grayscales of the regions in Fig. 14(a) are 96.83, 101.42, 101.85, 126.67, 155.81, 158.02, 23.355, and 15.55. Compared to the total transmittances, a proportional relationship is observed except for "G."

We assumed that the relationship between the grayscale and transmittance of bird droppings was sigmoid. Fig. 15 shows the dependence of the transmittance curve on the grayscale fitted by a sigmoid function. An equation of the curve is expressed in (16); T_r denotes transmittance with a percent unit, α_t and β_p denote fitting parameters, and γ_N denotes a light noise parameter which implies external light sources. Physically, α_t means a transmittance gradient based on the grayscale and β_p means a starting point of bird droppings in grayscale without light noises. If a value of α_t is big, the transmittance curve has a gradual curve, which means a transition of grayscale could bring relatively small change of transmittance. Conversely, if a value of α_t is small, the transmittance curve has a gradual curve which means a transition of grayscale could bring relatively large change of transmittance. γ_N means a parallel translation of the transmittance curve by external light sources. Thus, a sum of β_p and γ_N indicates a general starting point of bird droppings in grayscale in an image, which corresponds to 78.2 in Fig.14(b)

$$T_r = \frac{100}{(1 + \exp(\alpha_t \cdot (G - (\beta_p + \gamma_N)))} . \tag{16}$$

C. Proposed Model and Power Prediction

Until now, we assumed that an additional photocurrent was generated in bird-dropping shades by penetrating light and verified that the PV output was larger in bird-dropping shades than that in hard shading. To model this phenomenon, the transmittance curve was used as the ratio of the photocurrent in the shaded region. Fig. 16 shows the equivalent circuit of the proposed BS. The difference in the proposed BS reflects the soft-shading effect. $I_{\mathrm{ph,sh}}$ denotes the photocurrent in the shaded region. $I_{\mathrm{ph,sh}}$ was calculated using (17), and the operating current of

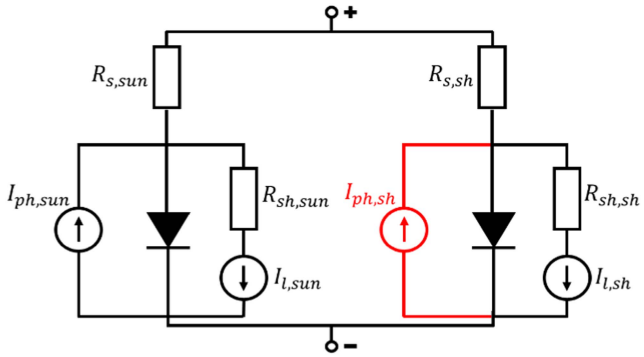

Fig. 16. Equivalent circuit of a proposed model.

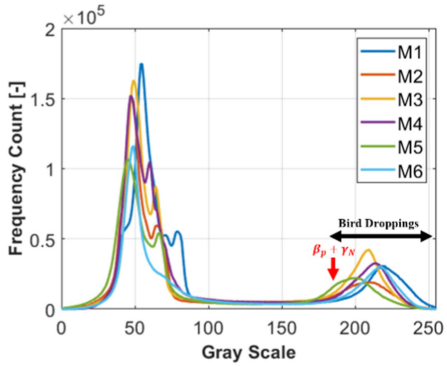

Fig. 17. Image histograms of the modules shaded by bird droppings.

the shaded region is modified using

$$I_{\text{ph,sh}} = I_{\text{ph}} \cdot \text{SR} \cdot \frac{T_r}{100} \tag{17}$$

$$I_{\text{sh}} = I_{\text{ph,sh}} - I_o \left\{ \exp\left(\frac{V + I_{\text{sh}} R_{s,\text{sh}}}{nV_T} \right) - 1 \right\} - I_{l,\text{sh}}. \tag{18}$$

The outputs of the contaminated modules were calculated using a transmittance curve. When the transmittance curve in Fig. 15 is calculated, γ_N assumes 0 because external light sources are minimized. However, the modules of Fig. 5 have external light sources on the upper sides of the modules, and we must consider diverse values of γ_N. This article does not present a method to quantify the effects of light sources, γ_N, but rather simply determines a value of γ_N using an image histogram.

Fig. 17 shows the image histograms of the gray images of Fig. 5. It can be observed that the starting points of bird droppings on the grayscale are located between 150 and 180. The values are larger than Fig. 14(b) because of external light sources. In this article, the value of the starting points of bird droppings is simply assumed as 160. However, some errors in γ_N should be expected depending on images due to performance differences of a camera.

Additionally, the position of the light source could lead to discordance in the light noise depending on the cell region. If an equal amount of light is projected in front of the module, the discordance should be neglected. However, the position of the light source is not ideal, and its effect (the discordance) varies depending on the position. Fig. 18 shows the average values of the grayscales in the nonshaded region. Fig. 18(a) presents a vertical analysis of the grayscale. Given that the top regions are near the light sources, the gray scale has a higher value than other regions. Furthermore, the gap is observed up to 30. The

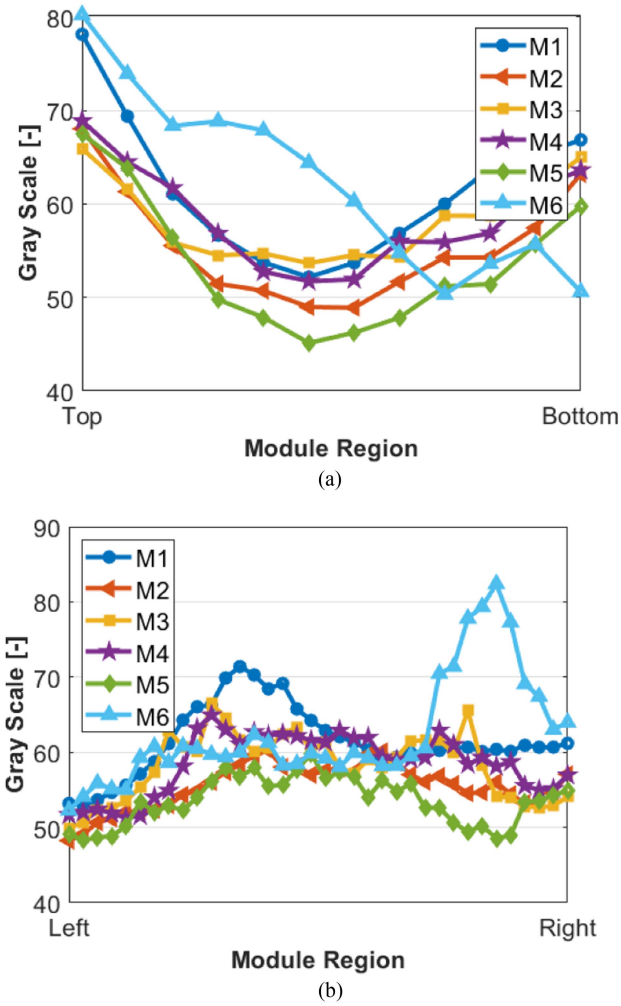

Fig. 18. Averaged grayscales in the nonshaded areas: (a) from top to bottom, and (b) from left to right.

grayscale decreased further away from the light sources. However, the grayscale rebounds near the bottom because of the light reflection from the white floor. Fig. 18(b) presents a horizontal analysis of the grayscales. We can identify the positions of external lights where the grayscales are heightened. The lights were positioned on both the left and right sides; notably, the light on the left influenced M1 to M5, while the light on the right had a substantial impact on M6. Consequently, Fig. 18 illustrates the variance in light noises depending on the location of the light sources. The transmittance curve should be applied variably influenced by the position of light.

Variations in light noise are applied by a correction value, as shown in (19). C_N denotes a correction value that eliminates variations in light noises depending on the location of the lights. A calculation of C_N is divided into two parts. First, we calculated the averaged grayscale in nonshaded areas according to cell regions; we obtained 432 values of the averaged gray scales. The C_N was then calculated by subtracting the minimum value from the averaged grayscales. Fig. 19 shows the results of C_N calculations based on the cell regions. The upper areas of the modules in Fig. 19 have larger C_N than those in other areas because of their proximity to the light sources. The lower areas also had relatively larger C_N because of light reflection from the white floor. Consequently, while C_N generally ranged from a minimum value of 0 to a typical maximum of 30–40.

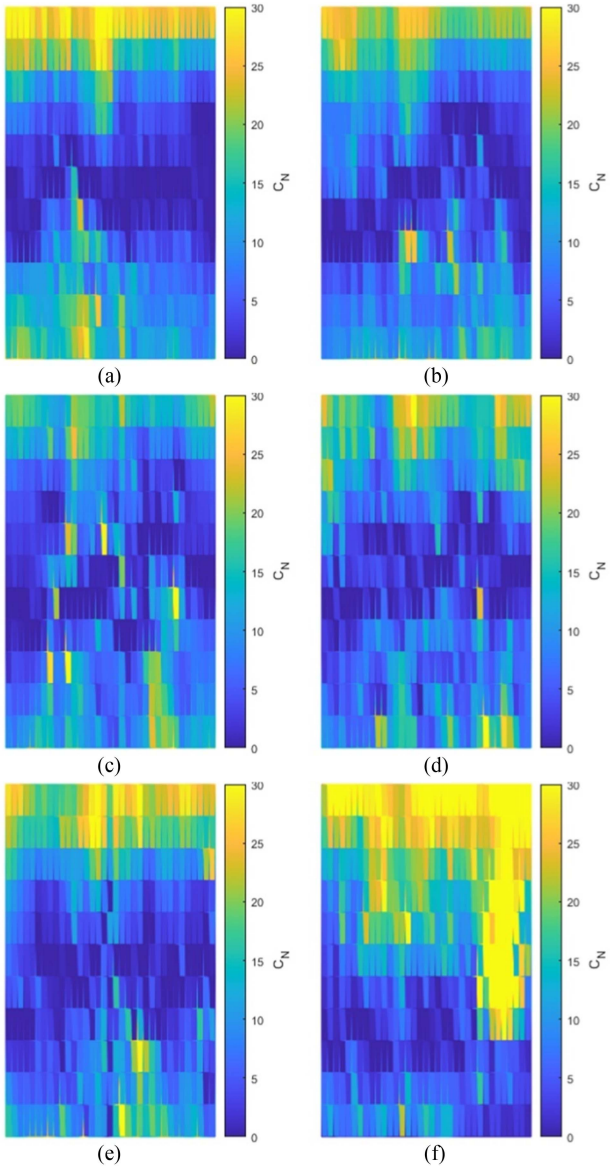

Fig. 19. Value of C_N with respect to cell regions: (a) M1, (b) M2, (c) M3, (d) M4, (e) M5, and (f) M6.

Also, some distortion values caused by undivided bird droppings exist. Undivided bird droppings occurs when bird droppings are too shallow to be separated by the image thresholding, and appears near the sorted bird droppings. The CN data in Fig. 19 have the distortion. "M1" to "M5" have sporadic distortions, but "M6" has a massive distortion region depending on the bird-dropping shades. This distortion would lead a transmittance and prediction overestimation, described in a following paragraph:

$$T_r = \frac{100}{(1+\exp(\alpha_t \cdot (G - (\beta_p + \gamma_N - C_N)))}. \tag{19}$$

Now, we predict the output of a module contaminated with bird droppings by considering the transmittances of bird droppings and light noise. The power predictions through the proposed model were taken identically shown in Fig. 8. The IV curves of the proposed model are shown in Fig. 20. The red lines represent the results of BS model, the black dotted lines represent the measured data, and the blue lines

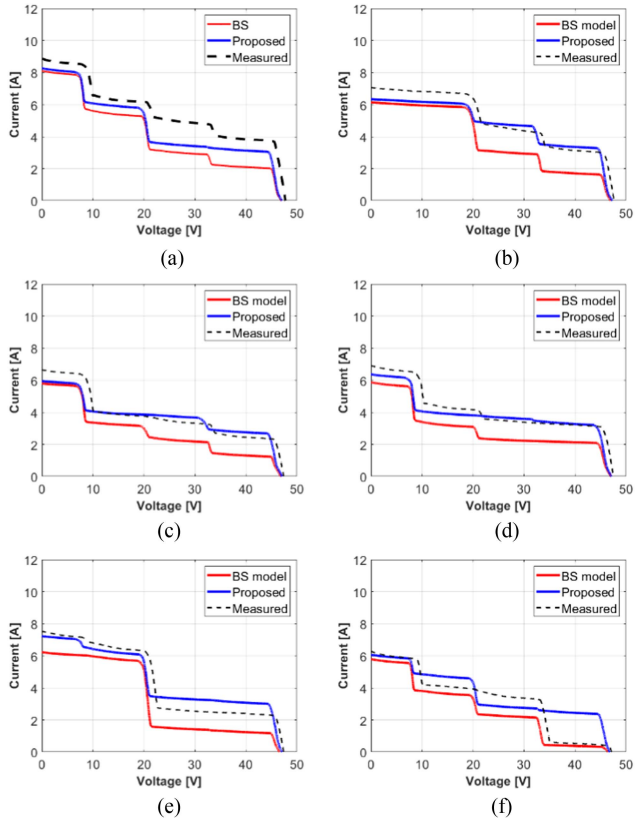

Fig. 20. IV curves of the proposed model: (a) M1, (b) M2, (c) M3, (d) M4, (e) M5, and (f) M6.

represent the results of the proposed model. In particular, the IV curves in the low-current regions were improved.

RMSE between IV curves is calculated to determine the similarity of the results to the measured value. RMSE is computed by deviations between the measured current and calculated current in the PV operational region ($V > 0$ and $I > 0$). If RMSE is relatively large, it means that the calculated IV curve is quite different with the measured one. Conversely, if RMSE is relatively low, it means that the calculated IV curve is similar with the measured one.

For M1, the RMSE values are 1.6206 A for BS model and 1.1303 A for the proposed model. Similarly, for M2, the RMSEs are 1.3411 and 0.6039 A for the BS and proposed models, respectively. M3's RMSE is 1.1152 A in BS model, contrasting with 0.5451 A in the proposed model. M4's values are 1.2656 A for the BS model and 0.6350 A for the proposed model, and M5's values correspond to 1.3091 A for the BS model against 0.6901 A for the proposed model. Although the prediction model is imperfect, the mismatch of IV curves and power prediction have improved by applying "soft shading."

However, M6 deviates slightly with an RMSE of 0.8929 A in the BS model, increasing to 1.0161 A in the proposed model, caused by the overestimated current at a high-voltage region (35–48 V). A reason for the overestimation is the large $I_{\mathrm{ph,sh}}$, which means that an excessive photocurrent is generated in the shaded region. We could find that "M6" had a huge bird dropping in one bypass section, see Fig. 5(f). This bird dropping causes a distortion of C_N, C_N denotes a positional light noise deviation based on the minimum, and leads to the prediction overestimation.

Table VIII describes a numerical analysis of Fig. 20 depending on cases. In all instances, the APE was lower than that of the BS

TABLE VIII
MAXIMUM POWER ANALYSIS OF THE PROPOSED MODEL

CASE	Predicted (W)	Measured (W)	Deviation (W)	APE (%)
M1	135.10	167.01	−31.91	19.11
M2	147.22	135.82	11.4	8.39
M3	118.68	103.08	15.6	15.13
M4	140.16	138.71	1.45	1.05
M5	133.44	127.02	6.42	5.05
M6	105.62	107.50	−1.58	1.47

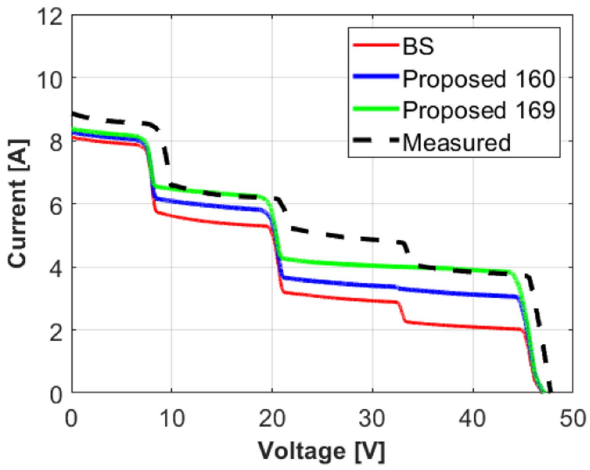

Fig. 21. IV curves of "M1."

model. Specifically, M1 experienced an 18.89% reduction in APE. Furthermore, M2, M3, M4, and M5 observed decreases in APE by 11.91%, 17.13%, 32.55%, and 10.25%, respectively. While M6 saw a substantial 33.83% decline in APE, it differed in its maximum power point.

V. CONCLUSION

This article analyzes the soft-shading properties of bird droppings and suggests a method to predict the output of a module contaminated by bird droppings. To identify the properties of bird droppings, we tested the transmittance of bird droppings with various samples and compared the bird-dropping shading with hard shading. A maximum of 10% of light penetrated the bird-dropping samples, and power differences of up to 40% were confirmed. This article proposes a power prediction method using the relationship between the grayscale and transmittance. The transmittance curve is fitted by the sigmoid function, and the proposed model is based on the BS. Despite the absence of light noise quantification, the proposed model offers better predictions for the outputs of modules affected by bird droppings compared to the BS model.

A problem of soiling is converted to optics (grayscale) from an environmental aspect (soiling accumulation). However, in future articles, following points should be considered. First, we assumed the same starting point (a sum of β_p and γ_N) of bird droppings to be a fixed value of 160 in all of the contaminated modules. However, this value varies based on camera performance and composition, and it is evident that each module picture has the different value. For example, the bird-dropping regions in the grayscale differ slightly in Fig. 17. In case of "M1," a value of 169 is optimal as the maximum power corresponds to 167.26 W and RMSE of an IV curve corresponds 0.7958 A. Fig. 21 describes the result. "Proposed 160" denotes the result of the proposed model with the value (a sum of β_p and γ_N) of 160, and "Proposed 169" denotes the result of the proposed model with the value of 169. Thus, although surroundings of an experiment are identical, instantaneous differences of camera performances can cause a transition of the value by up to 10, and should be quantified.

Second, this article complements variable light noise based on the grayscale of the nonshaded regions, C_N. However, a change in the grayscale in nonshaded regions is not equal to a change in the grayscale in shaded regions by external lights. This effect was most noticeable for M6 (Fig. 20). Because the positional light noise term had not generally defined, we used the grayscale of the nonshaded region for quantifying the light noise. Then, the power prediction is affected by the abnormal values, shown in Fig. 19. If a change in the grayscale owing to light source is generally **quantified**, then drawing an IV curve would be more accurate.

Third, some supplements are required before they are applied in practice. For example, moving light sources (sunlight) can generate time-varying light noise. The quantification and formulation of the time-variant light noise are required.

Finally, other soiling materials, such as dirt, could be adapted in the prediction model, especially in the transmittance curve. This article only analyzed the bird-dropping shades because it is the most remarkable hindrance of the marine modules. If other soiling samples are made, the analyses would be simply done with the described steps in this article. Also, except for the material type, the transmittance is also affected depending on a state of the material, such as water content [16]. Those factors would be analyzed in a view of the transmittance curve for better accuracy. Then, the transmittance curve could be significantly improved, and this article just propose a basic design.

A Marine environment, which covers almost 70% of the Earth's surface, is an important solution with respect to the lack of land availability. The greenhouse effect has caused rising sea levels, and some countries have insufficient land for installing PV systems. Marine PV systems can effectively address these problems. This article could provide a foundation for marine PV O&M by analyzing bird droppings.

ACKNOWLEDGMENT

The authors appreciate Chungbuk Technopark Next Generation Energy Center for the measurements and comments.

REFERENCES

[1] R. Cazzaniga and M. Rosa-Clot, "The booming of floating PV," *Sol. Energy*, vol. 219, pp. 3–10, 2021.
[2] N. Park, C. Han, and D. Kim, "Effect of moisture condensation on long-term reliability of crystalline silicon photovoltaic modules," *Microelectron. Rel.*, vol. 53, no. 12, pp. 1922–1926, 2013.
[3] L. Spinella et al., "Chemical and mechanical interfacial degradation in bifacial glass/glass and glass/transparent backsheet photovoltaic modules," *Prog. Photovolt.: Res. Appl.*, vol. 30, no. 12, pp. 1423–1432, 2022.
[4] M. Kumar, H. M. Niyaz, and R. Gupta, "Challenges and opportunities towards the development of floating photovoltaic systems," *Sol. Energy Mater. Sol. Cells*, vol. 233, 2021, Art. no. 111408.
[5] G. Rodriguez-Garcia, J. J. Kellar, Z. Zhu, and I. Celik, "Toxicity assessment of lead and other metals used in perovskite solar panels," in *Proc. IEEE 49th Photovolt. Specialists Conf.*, 2022, pp. 1284–1287.
[6] G. Oreski et al., "Properties and degradation behaviour of polyolefin encapsulants for photovoltaic modules," *Prog. Photovolt.: Res. Appl.*, vol. 28, no. 12, pp. 1277–1288, 2020.
[7] F. De Angelis, "The prospect of lead-free perovskite photovoltaics," *ACS Energy Lett.*, vol. 6, no. 4, pp. 1586–1587, 2021.
[8] E. Skuras et al., "Lead free ohmic connections on high efficiency silicon solar cells," in *Proc. 32nd Eur. Photovolt. Sol. Energy Conf.*, 2016, pp. 20–24.

[9] T. Hooper, A. Armstrong, and B. Vlaswinkel, "Environmental impacts and benefits of marine floating solar," *Sol. Energy*, vol. 219, pp. 11–14, 2021.
[10] S. Suzuki et al., "Acceleration of potential-induced degradation by salt-mist preconditioning in crystalline silicon photovoltaic modules," *Jpn. J. Appl. Phys.*, vol. 54, no. 8S1, 2015, Art. no. 08KG08.
[11] F. Setiawan, T. Dewi, and S. Yusi, "Sea salt deposition effect on output and efficiency losses of the photovoltaic system; a case study in Palembang, Indonesia," *J. Phys.: Conf. Ser.*, vol. 1167, Feb. 2019, Art. no. 012028.
[12] R. Claus and M. López, "Key issues in the design of floating photovoltaic structures for the marine environment," *Renewable Sustain. Energy Rev.*, vol. 164, 2022, Art. no. 112502.
[13] T. T. E. Vo, H. Ko, J. Huh, and N. Park, "Overview of possibilities of solar floating photovoltaic systems in the offshore industry," *Energies*, vol. 14, no. 21, 2021, Art. no. 6988.
[14] A. Vasiliu and D. Buruiana, "Are birds a menace to outdoor monuments," *Int. J. Conservation Sci.*, vol. 1, no. 2, pp. 83–92, 2010.
[15] M. Piliougine, J. Carretero, M. Sidrach-de-Cardona, D. Montiel, and P. Sánchez-Friera, "Comparative analysis of the dust losses in photovoltaic modules with different cover glasses," in *Proc. 23rd Eur. Sol. Energy Conf.*, 2008, Art. no. 2698e2700.
[16] Y. N. Chanchangi, A. Ghosh, S. Sundaram, and T. K. Mallick, "An analytical indoor experimental study on the effect of soiling on PV, focusing on dust properties and PV surface material," *Sol. Energy*, vol. 203, pp. 46–68, 2020.
[17] M. Coello and L. Boyle, "Simple model for predicting time series soiling of photovoltaic panels," *IEEE J. Photovolt.*, vol. 9, no. 5, pp. 1382–1387, Sep. 2019.
[18] B. Laarabi, Y. El Baqqal, A. Dahrouch, and A. Barhdadi, "Deep analysis of soiling effect on glass transmittance of PV modules in seven sites in Morocco," *Energy*, vol. 213, 2020, Art. no. 118811.
[19] B. Figgis, A. Ennaoui, S. Ahzi, and Y. Rémond, "Review of PV soiling particle mechanics in desert environments," *Renewable Sustain. Energy Rev.*, vol. 76, pp. 872–881, 2017.
[20] A. K. Sisodia and R. K. Mathur, "Impact of bird dropping deposition on solar photovoltaic module performance: A systematic study in Western Rajasthan," *Environ. Sci. Pollut. Res.*, vol. 26, no. 30, pp. 31119–31132, 2019.
[21] A. E. M. Fodah et al., "Performance evaluation of solar photovoltaic panels under bird droppings accumulation using thermography," *MRS Energy Sustainability*, pp. 1–11, 2024. [Online]. Available: https://www.researchsquare.com/article/rs-3179348/v1
[22] M. Aghaei, A. Gandelli, F. Grimaccia, S. Leva, and R. E. Zich, "IR real-time analyses for PV system monitoring by digital image processing techniques," in *Proc. Int. Conf. Event Control, Commun., Signal Process.*, 2015, pp. 1–6.
[23] V. S. Bharath, A. Kurukuru, and M. A. Khan, "Fault classification for photovoltaic modules using thermography and image processing," in *Proc. IEEE Ind. Appl. Soc. Annu. Meeting*, 2019, pp. 1–6.
[24] M. W. Akram et al., "Improved outdoor thermography and processing of infrared images for defect detection in PV modules," *Sol. Energy*, vol. 190, pp. 549–560, 2019.
[25] M. Karakose and M. Baygin, "Image processing based analysis of moving shadow effects for reconfiguration in PV arrays," in *Proc. IEEE Int. Energy Conf.*, 2014, pp. 683–687.
[26] T. G. Amaral, V. F. Pires, and A. J. Pires, "Fault detection in PV tracking systems using an image processing algorithm based on PCA," *Energies*, vol. 14, no. 21, 2021, Art. no. 7278.
[27] W. K. Yap, R. Galet, and K. C. Yeo, "Quantitative analysis of dust and soiling on solar PV panels in the tropics utilizing image-processing methods," in *Proc. Asia-Pacific Sol. Res. Conf.*, 2015.
[28] H. Qasem, A. Mnatsakanyan, and P. Banda, "Assessing dust on PV modules using image processing techniques," in *Proc. IEEE 43rd Photovolt. Specialists Conf.*, 2016, pp. 2066–2070.
[29] S. Fan et al., "A deep residual neural network identification method for uneven dust accumulation on photovoltaic (PV) panels," *Energy*, vol. 239, 2022, Art. no. 122302.
[30] S. Fan et al., "A novel image enhancement algorithm to determine the dust level on photovoltaic (PV) panels," *Renewable Energy*, vol. 201, pp. 172–180, 2022.
[31] C. E. Clement, J. P. Singh, E. Birgersson, Y. Wang, and Y. S. Khoo, "Illumination dependence of reverse leakage current in silicon solar cells," *IEEE J. Photovolt.*, vol. 11, no. 5, pp. 1285–1290, Sep. 2021.
[32] D. Liu and J. Yu, "Otsu method and K-means," in *Proc. 9th Int. Conf. Hybrid Intell. Syst.*, 2009, pp. 344–349.
[33] T.-H. Kang, S.-H. Kim, S.-D. Jin, H.-J. Cho, and W.-K. Paek, "The study for grading of the saemangeum by birds," *Korean J. Ornithol.*, vol. 18, no. 3, pp. 181–189, 2011.
[34] R. G. Vieira, F. M. de Araújo, M. Dhimish, and M. I. Guerra, "A comprehensive review on bypass diode application on photovoltaic modules," *Energies*, vol. 13, no. 10, 2020, Art. no. 2472.
[35] S. Silvestre, A. Boronat, and A. Chouder, "Study of bypass diodes configuration on PV modules," *Appl. Energy*, vol. 86, no. 9, pp. 1632–1640, 2009.
[36] R. G. Vieira, F. M. de Araújo, M. Dhimish, and M. I. Guerra, "A comprehensive review on bypass diode application on photovoltaic modules," *Energies*, vol. 13, no. 10, 2020, Art. no. 2472.
[37] N. M. A. A. Shannan, N. Z. Yahaya, and B. Singh, "Single-diode model and two-diode model of PV modules: A comparison," in *Proc. IEEE Int. Conf. Control Syst., Comput. Eng.*, 2013, pp. 210–214.
[38] V. Quaschning and R. Hanitsch, "Influence of shading on electrical parameters of solar cells," in *Proc. Conf. Rec. 25th IEEE Photovolt. Specialists Conf.*, 1996, pp. 1287–1290.
[39] N. Klasen, D. Weisser, T. Rößler, D. H. Neuhaus, and A. Kraft, "Performance of shingled solar modules under partial shading," *Prog. Photovolt.: Res. Appl.*, vol. 30, no. 4, pp. 325–338, 2022.
[40] N. M. F. T. S. Araújo, F. J. P. Sousa, and F. B. Costa, "Equivalent models for photovoltaic cell—A review," *Revista de Engenharia Térmica*, vol. 19, no. 2, pp. 77–98, 2020.